A High-Resolution Portable Gamma-Camera for Estimation of Absorbed Dose in Molecular Radiotherapy

T. Bossis, M.-A. Verdier, C. Trigila, L. Pinot, F. Bouvet, A. Blot, H. Ramarijaona, T. Beaumont, D. Broggio, O. Caselles, S. Zerdoud, and L. Ménard

Abstract—**Molecular radiotherapy is a treatment modality that requires personalized dosimetry for efficient treatment and reduced toxicity. Current clinical imaging systems and miniaturized gamma-cameras lack the necessary features for this task. In this article, we present the design and optimization of a mobile gamma-camera with a 10×10 cm^2 field of view tailored for quantitative imaging during ^{131}I therapy of thyroid diseases. The camera uses a monolithic $10 \times 10 \times 1$ cm^3 CeBr$_3$ scintillator coupled to a 16×16 SiPMs array and commercial electronics. It exhibits high imaging performance with an intrinsic spatial resolution (SR) of 1.15-mm FWHM, an energy resolution of 8% FWHM at 356 keV and negligible deadtime up to 150 kcps. Images are reconstructed in real time using a convolutional neural network. The manufacturing method of tungsten collimators and shielding was optimized using laser 3-D printing to achieve an effective density of 97% that of bulk tungsten. Their geometry was adjusted with Monte-Carlo simulations in order to reduce septal penetration and scattering and optimize the signal-to-noise ratio at short times after treatment administration. Two high-energy parallel-hole collimators with high sensitivity or very high SR were designed for treatment planning and post-treatment control. The fully operational gamma-camera will soon be clinically assessed.**

Index Terms—**Dosimetry-guided radionuclide therapy, high performance, mobile gamma-camera, quantitative image, thyroid diseases.**

I. Introduction

IN THE last years, molecular radiotherapy has been under strong development in order to reach highly targeted delivery of the treatment and theranostic approaches, with huge gain in treatment efficiency. These improvements were first obtained by the development of new beta or alpha emitting radionuclides and more specific radiopharmaceuticals, as for instance ^{177}Lu-DOTATATE for neuroendocrine tumors [1], ^{225}Ac-PSMA for metastatic castration-resistant prostate cancers [2], or ^{111}In-CP04 for medullary thyroid cancers [3]. However, ^{131}I is still the most widespread radiopharmaceutical, with 84% of European patients treated for malign and begnin thyroid diseases [4]. As with conventional radiotherapy, these advances also further emphasize the need of a good assessment of the delivered dose to targeted tissues and organs-at-risk for each patient [5]. Patient-specific dosimetry is the key to reach the highest reasonably achievable treatment efficiency by establishing precise correlation between the absorbed dose and the biological response [6]. The expected benefits are the adjustment of the activity to be administered according to the desired treatment outcomes and the tolerance doses of organs-at-risk. For the treatment of thyroid diseases with ^{131}I, this includes the destruction of tumor residues, the restoration of thyroid function, the reduction of hypothyroidism, or the limitation of side-effects on salivary glands function (xerostomia) [7], [8].

The individual estimation of the absorbed dose is based on the measurement of activity biodistribution over time [5]. The biokinetics of the radiopharmaceutical is usually estimated from accurate quantitative imaging of the target organ and organs-at-risk several times after administration of a low amount of tracer activity. This planning phase allows to set the therapeutic activity to be administered according to the absorbed dose estimation. After administration of therapeutic activity ranging from few hundreds MBq to several GBq, quantitative imaging over time is used to ensure that the real delivered dose corresponds to the prescribed dose [7], [8]. The use of quantitative imaging-based dosimetry for personalizing molecular therapy requires the imaging device to have several features that are not or only partially provided by existing large field-of-view (FOV) gamma-cameras, which are mainly designed for diagnosis examinations. This includes detection of high-energy gamma-rays (up to 600 keV), high spatial resolution (SR) to improve detectability and activity quantification of small heterogeneities by reducing partial volume effect, high energy resolution to reduce contribution from scattered high-energy gamma-rays, high counting rate capability for early imaging after treatment administration, compactness to improve image contrast by reducing the distance from the source and to optimize the angular view,

and finally mobility, to perform exams at the patient's bedside or in an isolated room for an accurate temporal sampling of the radiopharmaceutical biokinetics. Currently available wide field gamma-cameras equipped with high-energy lead collimators exhibit poor SR, ranging from 1 to 2 cm at a 10-cm distance, and low-image contrast when using high-energy gamma-rays [9], [10]. Moreover, their availability and their space requirements reduce the possibility of carrying out several measurement points in time. To address this availability issue, industrial manufacturers have developed small mobile gamma-cameras, such as Picola Scintron (MiE Medical Imaging Electronics), SoloMobile (DDD-Diagnostic), or Nucline (Mediso). Their interest lies in the possibility of freeing up whole body scanners by providing an alternative for diagnostic planar imaging of single organs, such as thyroid, bones, or sentinel nodes [11]. However, these cameras are generally limited to diagnostic examinations with low-energy emitters, such as ^{123}I or ^{99m}Tc. Furthermore, even though their FOV is considered small (down to 20×20 cm^2), it is still too large to optimize image capture of the thyroid. In the last years, some novel miniaturized gamma-cameras have also been developed [12], [13], [14], [15]. A lot of efforts have been put in the reduction of the size and weight of the imaging devices, thanks to the development of new photodetectors, such as silicon photomultipliers (SiPMs) and the integration of their readout electronics. However, a large majority of those cameras are designed for intraoperative imaging applications, once again using low-energy emitters and relatively low activities in the MBq range. Their detection design, and in particular, the collimator geometry, is not suited to ^{131}I imaging, which has two main gamma emission lines at 364 and 637 keV (83% and 7%, respectively). Their counting rate capabilities and shielding efficiency are also too low for early imaging during the treatment of thyroid diseases, shortly after administration of several GBq of ^{131}I [13]. Finally, the FOV of these prototypes is too small to fit the size of adults thyroid or enlarged thyroid of some pathological cases.

In that context, our objective is to develop a high-resolution portable gamma-camera specifically optimized to accurately measure the biokinetics of ^{131}I at the patient's bedside during treatment planning and post-treatment therapeutic dose verification of malign and benign thyroid diseases. A first proof-of-concept prototype with a 5×5 cm^2 FOV has already been developed and allowed to validate the feasibility of such an imaging device [16]. It showed very good intrinsic performance, with an energy resolution of 7.86% at 364 keV and a submillimetric intrinsic SR of 0.61-mm full-width at half-maximum (FWHM). Its quantification ability has been evaluated on thyroid phantoms with excellent results, mainly thanks to its high SR, which both mitigates the partial volume effect and gives access to precise anatomical information on the size or depth of targeted structures. We are now aiming to develop a high-resolution mobile gamma-camera suited to clinical environment with a 10×10 cm^2 FOV, enhanced counting capabilities for imaging with high photon fluences up to several GBq and interchangeable collimators suitable for both planning and post-treatment control. In this article, we will present the optimization studies carried out on the
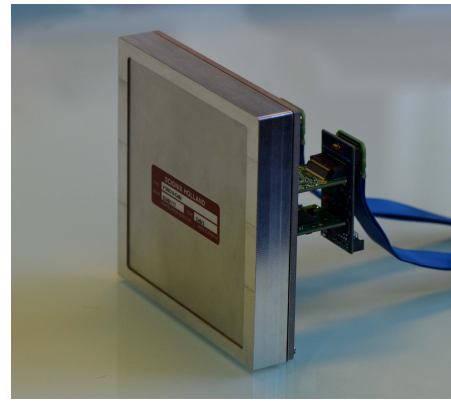

Fig. 1. Gamma detection module of the camera. The monolithic scintillator is coupled to the SiPMs array, which is plugged to two front-end readout electronic modules via a custom adaptation board.

different components of this new gamma-camera, including the photodetection system, collimator, and shielding, specifically designed to meet the need for accurate quantification of ^{131}I biodistribution and kinetics, particularly in small heterogeneities.

II. Design of the Mobile Gamma-Camera

The design of the gamma-camera consists in a 10×10 cm^2 and 1-cm thick CeBr$_3$ monolothic scintillator coupled to an array of 16×16 SiPMs readout by a 256-channels miniaturized electronics (Fig. 1). The projected image of the gamma-ray distribution on the surface of the scintillator is formed by a high-energy parallel-holes tungsten collimator. The whole camera is shielded from background radiations with tungsten and lead plates. The external dimensions of the detection head are about $20\times20\times25$ cm^3 for a total weight of 50 kg (Fig. 2, left and center). A mobile mechanical structure equipped with a motorized telescopic column enables the easy positioning of the camera at patient level. The tilt of the detection head can also be adjusted manually (Fig. 2, right).

A. Scintillator–Photodetector System

The design of the photodetection system of the clinical prototype is shown in Fig. 1. It consists of an array of 4×4 Hamamatsu S13361-6050NE-04 matrices with 4×4 pixels (SiPMs). Each pixel has a sensitive area of 6×6 mm^2 and a microcell pitch of 50 μm, for a total of 14 336 microcells per pixel. The dead space between pixels is 0.2 and 0.4 mm at the junction of two matrices. The photosensitive area of the array is 92.2 cm^2 for an overall area of 100 cm^2. The optical window of the arrays is made of an epoxy resin with a refractive index of 1.55. The SiPMs arrays are connected to the front-end electronics via a custom connection board. This PCB conveys high voltage from the ASICs to the SiPMs. The readout of SiPMs is made by four PETsys Electronics TOFPET2B ASICs boards, called FEB/A (two FEB/I boards interfacing two FEB/A each, Fig. 1), for a total of 256 analog channels. Each channel has its own independent trigger system composed of two branches for timing and energy measurements. The time branch uses a high-gain amplifier and
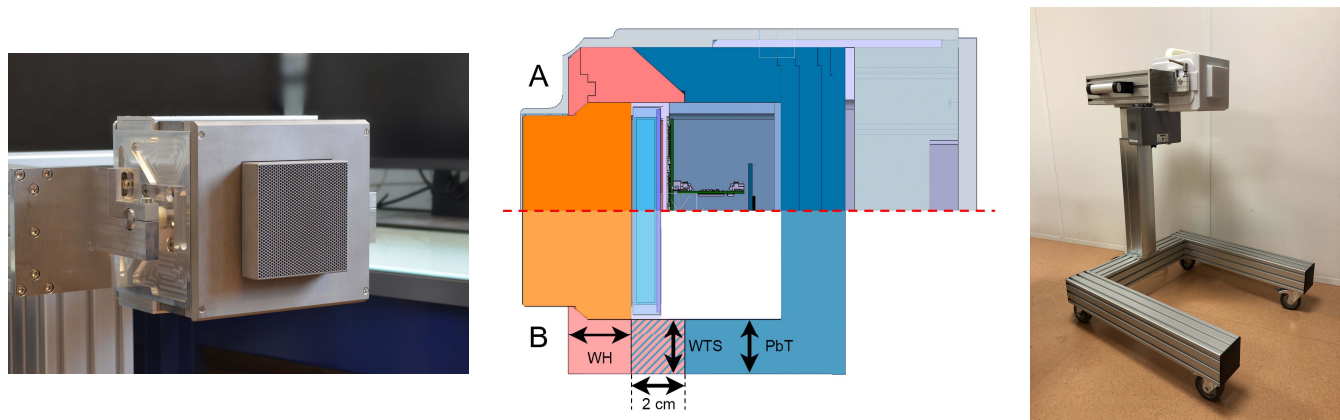
Fig. 2.   Left: Detection head of the mobile gamma camera. Center: (a) Cross section view of the detection head. Orange is the tungsten collimator, pink is the tungsten shielding, and dark blue is the lead shielding. The scintillator (light blue) is coupled to the SiPMs array and the electronics held in an aluminium housing. The light gray area represents the plastic case that covers the entire camera and houses the air-cooling system at the rear. (b) Schematic cross section view of the shielding geometry used for simulations. WH is the tungsten height on the front of the camera, PbT is the lead thickness on the back and sides of the camera, and the hatched area covering the sides of the scintillator is either lead with PbT thickness (WTS=0) or tungsten (WTS=PbT). Right: Mobile mechanical structure holding the detection head for its positioning at patient level.

two trigger thresholds, a low timing measurement trigger, and a higher trigger to reject dark counts without dead time and start charge integration. If the signal is above the trigger threshold of the energy branch, which features a lower gain amplifier for a wider range of signals before saturation, the event is then digitized on a 10-bit ADC. The maximum event rate per channel is 500 kHz. A spatial coincidence trigger between different regions of the detector is set to virtually eliminate all dark noise. The matrices of SiPMs are divided into two groups, spatially distributed as a checkerboard thanks to the connection board. To be validated, an event must trigger the two groups in temporal coincidence (10-ns time window). The two FEB/I boards are connected to a FEB/D DAq board via LVDS lines. The FEB/D board transmits the data via Gigabit Ethernet (1 Gb/s) to the DAq computer. The FEB/D boards also incorporates an FGPA for programming the four high-voltage lines supplying the SiPMs from 5 to 100 V with an accuracy of 1 mV and setting the ASICs parameters. The light response uniformity of the SiPMs arrays was corrected by applying a multiplication factor on the charge content measured from the uniform irradiation of the photodetectors with a pulsed LED light source. The relative standard deviation across pixels decreases to 0.96%, compared to 12.8% without correction. In order to ensure the stability of the measurements, the temperature of the camera was monitored using four thermal sensors plugged on the connection board, and a thermal sensor located close to the ASIC in each front-end electronics module. The photodetection system and readout electronics are held in an aluminum housing with external dimensions of $11.8 \times 11.8 \times 6.1$ cm^3.

The photodetection system is coupled to a 10×10 cm^2 and 1-cm thick CeBr$_3$ monolithic scintillator encapsulated in a mechanical frame with a diffuse optical coating on the edges and top surface (Scionix) (Fig. 2, center). This inorganic scintillator exhibits a light yield of 60 photons per keV, a scintillation decay time of 18 ns, a density of 5.18 g.cm^{-3}, and a total absorption efficiency at 364 keV of 27% for a $10 \times 10 \times 1$ cm^3 crystal block [17]. The mechanical frame is

sealed with a 1.5-mm thick output quartz window, which is coupled to the SiPMs array with an optical grease (BC-630, refractive index of 1.46, Saint-Gobain). Due to its size, the monolithic scintillator was produced by cutting the crystal ingot following its main axis of growth. The heat produced by the electronics readout is extracted from the aluminium housing thanks to two fans creating an airflow in the camera (Fig. 2, center). This cooling prevents strong mechanical stress on the scintillator housing due to fast temperature variations and stabilizes the SiPMs temperature about 4 °C above ambient temperature.

B. High-Energy Collimators and Shielding

The high-energy collimator is made of tungsten and composed of hexagonal parallel-holes (Fig. 2, left). Two collimators were designed, one suited to treatment planning with low amount of tracer activity (high-sensitivity collimator) and another one for post-treatment control with high therapeutic activity (high-resolution collimator). The gamma detection module is shielded from the ambient background radiations with lead and tungsten plates, whose geometry has been optimized to maximise the signal-to-noise ratio (SNR) at short times after treatment administration while keeping the dimensions and weight of the detection head at reasonable values (Fig. 2, left and center). The collimators and tungsten shieldings were manufactured by Volum-e.

C. Events and Image Reconstruction

The raw data file at the output of the readout electronics is a list of triggers, called hits, produced independently by each channel. Each hit is characterized by a timestamp, a digitized charge, and the corresponding channel ID. A first algorithm is used to search for temporal coincidences of hits, which we call temporal clustering. A group of hits within a 60-ns time window is considered to be part of the same gamma-ray event. This time window has been determined experimentally and corresponds to the maximum time difference between hits
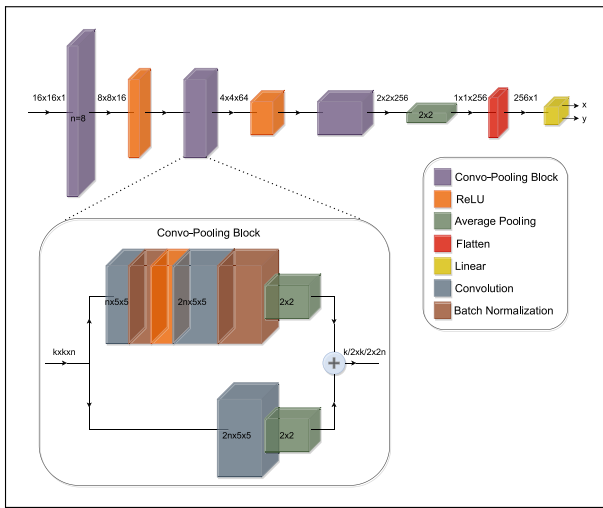
Fig. 3. Schematic view of the optimal deep residual CNN architecture and the detailed composition of a Convo-Pooling Block (see insert), with n the number of filters per layer and k the dimension of the square input image.

produced by the same gamma event, thus accounting for the jitter on the timestamp. We assume that the sum of the charge of each hit composing an event is proportional to the energy deposited in the scintillator by the incident gamma-ray.

An efficient image reconstruction algorithm based on a convolutional neural network (CNN) is used to accurately retrieve the interaction position in the scintillator from the measured 16×16 pixels charge distribution. It has been developed thanks to Keras Python's library and trained on an experimental dataset composed of 16×16 pixels measured charge distributions at known positions [18]. This dataset has been collected by scanning the scintillator surface with a 0.5-mm collimated ^{133}Ba source following a grid of 100×100 positions with a 1-mm step, registering around 2000 events per position at 356 keV (see Section III). Based on the work of Jaliparthi et al. [19], we used a *Deep Residual Convolutional* neural network composed of several *Convo-Pooling Blocks*. A CNN extracts spatial information by taking advantage of the fact that data produced by our detector are structured square images, with correlated content from a pixel to its neighbors. The *Convo-Pooling Block* structure, presented in Fig. 3, corresponds to the skip connection between the input and the output of two successive convolution layers followed by a pooling operation, and helps the neural network to learn faster and with more stability without adding complexity and trainable parameters [20]. After a systematic tuning of the hyperparameters and training settings described in [18], the optimal structure was found to be composed of three *Convo-Pooling Blocks*. The first block contains 8 and 16 5×5 filters on the first and second layer, respectively. The second block is identical but with 32 and 64 filters and the last block uses consecutively 128 and 256 filters. This optimal architecture is represented in Fig. 3. The network contains a total of around 1 million neurons. The training dataset size that gives the best results is 800 events per position (100×100 positions) with a step size of 1 mm. The mean absolute error loss function proved to offer better overall performance [18].

III. Investigation of the Intrinsic Performance of the Gamma-Camera

A. Spatial and Spectroscopic Intrinsic Performance

The intrinsic spectroscopic and spatial performance of the camera, including energy resolution and linearity, SR, local intrinsic spatial distortion (LISD), and uniformity, were assessed on the photodetection system coupled to the scintillator but without the parallel-holes collimator. The system was placed in a temperature controlled chamber kept at 21 °C and was irradiated with ^{133}Ba (356 keV) and ^{22}Na (511 keV) collimated sources. Two 3.3-cm thick tungsten collimators with a single 4 or 0.5 mm diameter hole were used for the evaluation of energy and spatial intrinsic performance, respectively. The positioning of the collimated sources were achieved by using a two-axis motorized platform with a position accuracy of 2 μm.

The trigger of the energy branch of the electronics readout cuts the tails of the charge distributions, and thus has a strong effect on the total collected charge. Therefore, the energy resolution at 356 keV was first optimized as a function of the trigger level of the energy branch and the overvoltage applied to the SiPMs by using a ^{133}Ba source centered on the FOV. A sum of four Gaussian functions was fitted on the main full-energy peaks of the ^{133}Ba energy spectra, that are 276, 303, 356, and 383 keV. The FWHM energy resolution was also evaluated on the whole FOV by scanning the scintillator surface with the ^{133}Ba source following a 20×20 positions grid with a 5-mm step, referred as the energy scan. Values extracted from the ^{133}Ba multiple Gaussian fit were used to compute the ADC units-to-keV conversion coefficient for energy resolution at 356 keV. The linearity of the energy response was then assessed with a collimated ^{22}Na acquisition and by plotting the number of fired pixels as a function of the calibrated energy and the collected charge. For each range of ten fired pixels, going from 0 to 256, spectra were obtained in terms of the number of fired pixels, energy, and collected charge. The median, the first, and the third quartiles are computed from each spectrum. A polynomial correction of the energy spectra nonlinearity is done by using three known gamma emission lines of ^{133}Ba (81, 303, and 356 keV) and 511-keV positron annihilation peak and 1275-keV gamma emission line of ^{22}Na. The FWHM energy resolution and the light intensity loss, defined as the relative variation of the photopeak position at 356 keV with respect to its highest position in the FOV, are represented as two 20×20 bins maps (pixel size of 5×5 mm^2). As specified by NEMA standards, mean value and standard deviation of the energy resolution were measured in the useful FOV (UFOV) corresponding to the full FOV of the camera, in the central FOV (CFOV) corresponding to 75% of the linear dimension of the UFOV, and in the complementary FOV ($\overline{\text{CFOV}}$) corresponding to the remaining surface uncovered by the CFOV [21]. To measure the energy resolution over the whole FOV, a flood-field uniformity acquisition was also performed by irradiating the FOV with an uncollimated ^{133}Ba source placed at 50 cm from the detector surface, recording 30 million events at 356 keV. A matrix of correction factors is created from the light intensity loss map to readjust the

356-keV peak position as a function of the interaction position. Energy resolution over the whole FOV is then extracted on the total corrected spectrum with a multiple Gaussian fit, as described above.

The spatial performance of the detector was investigated by using a 1-mm step scanning of the UFOV with the ^{133}Ba source collimated with the 0.5-mm diameter single-hole collimator from -49.5 mm to $+49.5$ mm in x and y directions from the center of the camera, resulting in a $100{\times}100$ positions grid. An energy window of two times the energy resolution is opened on the 356-keV photopeak. The dataset of measured $16{\times}16$ pixels charge distributions was cleaned from spurious events including gamma-rays that scattered in the scintillator by Compton interaction before being absorbed by photoelectric interaction, and delocalized events that penetrated through the collimator material. These events represent 1% and 77% of the events detected in the energy window, respectively. The filtering process is precisely detailed in [18] and leaves around 2k events recorded at 356 keV for each scan position. Half of this dataset was used for neural network training and the other half was used for measuring the camera's intrinsic performance, corresponding to its impulse response. The image of the reconstructed test dataset with a 1-mm step was fitted with a 2-D Gaussian function on each spot in order to calculate the mean reconstructed position and the standard deviation along the x and y directions for each scan position. The FWHM SR (SR_x and SR_y) along the x and y directions was calculated from these standard deviations by taking into account the local spatial linearity as presented in [16]. The FWHM was then obtained from a quadratic deconvolution of the single hole collimator diameter. The LISD was evaluated by performing a linear fit on the curve representing the mean reconstructed positions as a function of the true mechanical positions for each row (x direction) and column (y direction) of the scan, excluding the four outermost rows and columns to remain independent of edge effects. The distance in mm between the mean reconstructed position of each scan position and its best-fit value along x and y directions gives the LISD along x and y directions ($LISD_x$ and $LISD_y$). The intrinsic SR and LISD are represented in the form of two $100{\times}100$ maps, where each element corresponds the average value of SR_x and SR_y or the Euclidean norm of $LISD_x$ and $LISD_y$ in the associated $1{\times}1$ mm^2 area. The mean values and standard deviations of the intrinsic SR and LISD were also reported in the UFOV, CFOV, and $\overline{\text{CFOV}}$.

The flood-field uniformity acquisition was also used to measure spatial uniformity of reconstruction. As for energy resolution measurement, an energy correction was applied on the reconstructed data to account for variation in width and position of the 356-keV peak as a function of the interaction position. The peak position and energy resolution values measured with the $20{\times}20$ energy scan were used to set the position and width of the window for the energy cut on the reconstructed events of the flood-field acquisition as a function of their spatial position. The corrected image is resized to $100{\times}100$ pixels in order to reduce statistical fluctuation and blurred with a $3{\times}3$ pixels Gaussian convolution kernel. The integral and differential spatial uniformities were measured in the CFOV and $\overline{\text{CFOV}}$ from the corrected image. Considering the specificities of small FOV cameras (and especially their sensitivity to outliers), the integral uniformity (IU) was the ratio of the standard deviation of counts per image bin to the mean counts per image bin, as defined in [22]. The differential uniformity (DU) is calculated for each bin of the image from ten IU values as defined by NEMA, corresponding to the relative difference between the minimum and maximum value of counts over the 2, 4, 6, 8, and 10 nearest neighbor image bins along the x and y directions [21]. The mean of those values was used as a measure of DU.

B. Counting Rate Performance

The assessment of the detector deadtime over a wide range of activities corresponding to expected values encountered during treatment planning or post-treatment verification is an important procedure for calibration of quantitative imaging systems. In accordance with the operating principle of the trigger system of PETsys TOFPET2B ASICs, whereby one analog channel independently triggers and digitizes the integrated charge if it exceeds the trigger level of the energy branch, the number of hits for one gamma-ray interaction in the scintillator will depend on the deposited energy and location of the interaction. This means that electronics occupancy depends both on the measured count rate, the energy spectrum and therefore the energy of the incident gamma-rays and the activity concentration of the source. Usually, dead time assessment is done by using the decaying source method, which requires acquisitions during at least ten periods of the radionuclide used [23]. This method is not applicable with ^{131}I due to its half-life of eight days. A more convenient method is to place a point source at different distances from the scintillator. A ^{133}Ba point source was centered on the FOV of the camera without collimator and placed at distances ranging from 11 to 45 cm with a 2-cm step. The uncertainty on the source position with respect to the scintillator is ± 1 mm. The number of detected events within the whole energy spectrum was measured at each distance. A Monte-Carlo simulation of the experiment setup was implemented with the GATE simulation toolkit in order to estimate the expected count rate at each distance without deadtime [24]. The scintillator was modeled with its aluminium housing as well as the ^{133}Ba point source in its metallic case. Main emission lines of ^{133}Ba (79, 81, 276, 302, 356, and 383 keV) were considered. The counting rate capability of the camera was evaluated from the comparison of the measured and expected counting rates. The influence of the dead time on the charge collection and thus, on the energy performance was also evaluated by measuring the energy resolution at 356 keV for each source distance. The energy resolution was extracted from the energy-corrected flood-field images measured at each distance, as described in Section III-A. The mean energy resolution over the whole FOV at low counting rate was assessed from the scan performed to measure intrinsic spatial performance (see Section III-A).

C. Influence of Temperature

The breakdown voltage of SiPMs is sensitive to their operating temperature. Therefore, the bias voltage must be adjusted according to the temperature measured close to the photodetectors, in order to keep constant the gain, the photodetection efficiency and the cross-talk and afterpulses probability and thus, the spatial and energy performance of the camera. The fully integrated detection head equipped with the high sensitivity collimator (see Section V-E) was placed in a climatic chamber set at 21 °C and irradiated with the ^{133}Ba source placed in direct contact with the collimator, in order to measure the 356-keV photopeak position at the optimal overvoltage of 7.5 V (see Section V-A). The climatic chamber temperature set point was then varied from 17 °C to 31 °C, with a 2 °C step and a precision of ±0.1 °C. At each temperature, the photopeak position at an overvoltage of 7.5 V was measured and the bias voltage was adjusted in order to bring the photopeak back to the position measured at 21 °C. For each temperature, the energy resolution at 356 keV was measured with and without correction of the bias voltage.

IV. Optimization of the Detection Head

The parallel-hole collimator is the key element of the camera. When imaging high-energy gamma-rays emitted by ^{131}I, septal penetration and scattering in the collimator become prominent components that result in a loss of image contrast and distortion of the activity quantification [10]. Our mobile camera will also be used to estimate the biokinetics of ^{131}I from images acquired just after treatment administration, where activities can reach several GBq [7]. It is therefore mandatory to protect the camera from background radiation in order to prevent contamination of the quantification. The design of the collimator and shielding of the mobile camera were optimized for ^{131}I imaging with Monte-Carlo simulations by using the GATE Toolkit [24].

A. Additive Manufacturing Process

The half-value layer of tungsten at 356 keV is 28% less than that of lead, making it a perfect candidate for the design of high-energy collimators or shieldings [25]. Its high stopping power allows to reduce the septal thickness and the collimator length and thus to optimize its SR and sensitivity while reducing penetration and scattering [26]. Recent 3-D-printing methods, such as selective laser melting (SLM), open up new prospects for the construction of tungsten collimators, overcoming the limitations of conventional machining processes [27]. It consists in a high-power laser selectively melting thin tungsten powder, layer after layer. This process allows for very precise manufacturing, but if the printing parameters are not properly adjusted, the printed material will contain many open and closed porosities and its effective density could be much lower than the actual density of tungsten [28], [29], [30]. Several tungsten samples ($1 \times 1 \times 0.5$ cm^3) with different machine parameters were printed in order to minimize the porosities as much as possible and reach the highest density achievable. This includes printing baseplate preheating, the laser scanning speed and laser power, the thickness of tungsten powder layers, and the powder spreading technique. We made sure that these parameters do not affect the resulting dimensions of the printed parts. The tungsten powder used for all samples has a grain size ranging from 5 to 25 μm. The effective density of the samples, also called envelope density, was measured with mercury intrusion porosimetry (MIP). MIP consists in injecting liquid mercury under pressure into the tungsten sample, allowing to measure the envelope volume at low pressure and skeletal volume at high pressure, thus giving access to the volume occupied by the porosities [31]. The sample is then weighted to obtain its effective density.

B. Collimator Geometry

When designing a low-energy collimator, analytical models based on geometrical considerations are used to optimize the different dimensions, including septal thickness, hole diameter, and collimator length [32], [33], [34]. Those models are no longer suitable for imaging with high-energy gamma-rays, since they do not include realistic modeling of septal penetration and scatter inside the collimator material. The two collimators geometry of the mobile camera were therefore optimized using Monte-Carlo simulations and a specific focus was made on the spatial and energy distributions of penetration and scatter events from high-energy gamma-rays. The collimator geometry was modeled with the density of bulk tungsten (19.3 g.cm^{-3}). The design of the collimator was investigated with a 10-cm long ^{131}I line source with the five main gamma emission lines of ^{131}I (80, 284, 364, 637, and 722 keV). The source was placed at a source-to-collimator distance of 5 cm and tilted by 24° with respect to the x-axis of the collimator. The position, energy, and direction along the three axis of each gamma-ray entering and passing through the collimator was registered. The energy of each event is blurred with a Gaussian probability density function, whose standard deviation is set to obtain a high energy resolution of 2.5% FWHM at 364 keV in order to study the intrinsic properties of the collimator, independently of instrumental performance. Only events belonging to a 5% energy window around the 364-keV emission were selected. Four classes of events passing through the collimator have been defined according to their position and energy reported by GATE (Fig. 4). In this classification, the collimator unit is equal to that of a hole plus a septa: E1) *Nonscattered geometric* events are gamma-rays that enter the collimator through one of its units and exit through the same unit, E2) *Nonscattered nongeometric* events also called penetration events correspond to gamma-rays entering the collimator through one unit and exiting through another unit by penetrating one or more septa, E3b) *Scattered geometric* events enter and exit the collimator through the same unit but scatter on the inner surface of the hole, and E3a) events that enter the collimator by a unit and exit the collimator through another unit after scattering inside the collimator are called *Scattered nongeometric* events. The collimator length was adjusted from 3 to 6.5 cm in 0.5 cm steps, the hole diameter from 0.5 to 4.5 mm in 0.25 mm steps, and the septal thickness from 0.75 to 3.25 mm in 0.125 mm
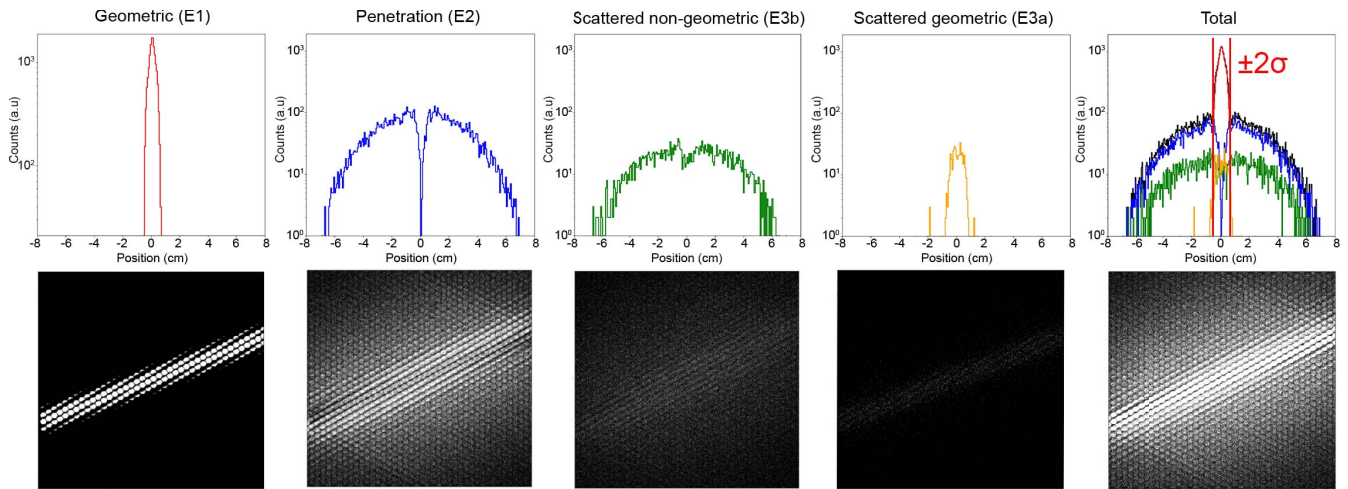
Fig. 4. Simulated spatial distribution of geometric, penetration, and scattered nongeometric and geometric events passing through a collimator irradiated with a ^{131}I line source (collimator length of 3.5 cm, septal thickness of 0.875 mm, and hole diameter of 2.25 mm).

steps. Each collimator geometry is evaluated in terms of its SR, useful efficiency (uE), and effective septal penetration (eSP). The collimator SR was calculated from a double Gaussian fit adjusted on the vertical profile obtained from the integration of the line source image along the x direction by taking into account the angular offset. The SR value was extracted from the FWHM of the central Gaussian, which mainly depends on the geometric components. Fig. 4 shows an example of a spatial profile together with the contributions of geometric (E1+E3a) and nongeometric events (E2+E3b). As can be qualitatively noticed, all geometric events are included in a $\pm 2\sigma$ ROI around the spatial peak profile, together with a small part of the nongeometric events. This fraction of nongeometric contribution does not degrade image quality and even contributes to increased efficiency. The uE was defined as the number of events detected within a region of $\pm 2\sigma$ around the line source image, divided by the number of 364 keV gamma-rays emitted by the source. By removing a large part of the nongeometric component, uE is more representative of the real efficiency of the collimator, i.e., the events that will contribute to the image formation and thus, to the quantification. The eSP was defined as the ratio between all the nongeometric events outside a region of $\pm 2\sigma$ around the line source image and the total number of detected events. Among all evaluated configurations, only those with a low eSP were selected for our application. We chose to set the eSP threshold to 7.5%. The minimum septal thickness to reach this value was extrapolated from the curves of eSP as a function of the septa thickness, as shown in Fig. 5. The result is a family of new geometric configurations, characterized by combinations of hole diameter, collimator length, and septal thickness allowing to achieve a 7.5% eSP. Interpolations methods were used to extend this finite number of simulated configurations to various septal thicknesses, hole diameters, and collimator lengths. Because SR and uE are not or only slightly influenced by penetration and scatter, these parameters show a general good agreement with the geometric analytical models developed for low-energy imaging [33] (Fig. 15).
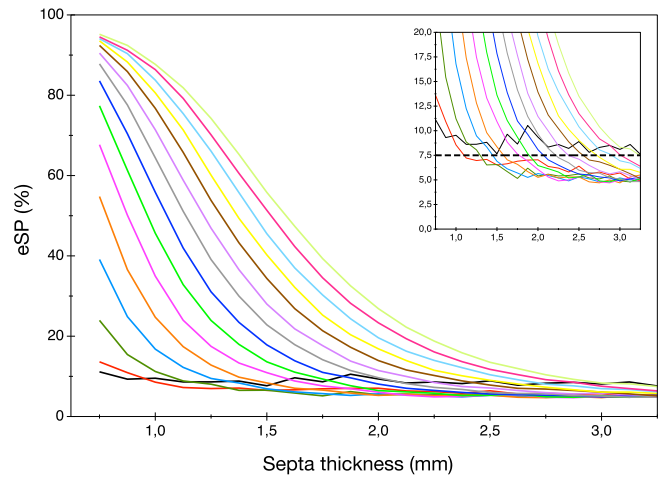

Fig. 5. Effective septal penetration eSP as a function of the hole diameter and septal thickness for a 4.5-cm collimator length. Each colored line corresponds to a hole diameter from 0.5 mm (black) to 4 mm (green) in 0.25 mm steps. The insert shows the determination of the minimum septa thickness to reach the 7.5% eSP threshold.

These models were therefore used to calculate the SR and uE values for all interpolated configurations.

C. Shielding Geometry

The shielding of the camera was optimized in order to limit the contamination from background radiations while keeping the dimensions of the camera as small as possible to facilitate its positioning in contact with the patient's neck. A clinically realistic simulation of a thyroid examination integrating the full design of the camera except the photodetection system and radioiodine uptake in the patient organs over time was modeled. The optimized high-resolution configuration of the collimator was simulated in order to consider the worst case in terms of SNR (see Section V-E). A schematic view of the shielding geometry used for simulations is shown in Fig. 2 (center, b). It included a tungsten plate on the front of the

camera (pink area, WH=2 or 3 cm), lead or tungsten covering the sides of the scintillator (hatched area, WTS=0, 2, or 3 cm), and lead covering the rest of the sides and back of the camera (PbT=2 or 3 cm). A reference shielding with all the materials set to an infinite density was also simulated for comparison. The density of tungsten was set at 18.0 g.cm^{-3} in order to take into account the typical effective density that can be reached with SLM printing methods (see Section II). The intrinsic energy resolution of the camera was set to 8% FWHM at 364 keV according to experimental results. The interaction positions of gamma-rays in the scintillator correspond to the barycenter of the energy deposits positions in the medium. The sources of background radiations inside the patient were modeled with the XCAT voxelized phantom [35]. The main uptake area of ^{131}I was simulated, including thyroid, stomach (content and wall), liver, kidney, blood iodide, small intestine, colon, adipose tissue, and muscle. No activity was considered in the bladder. The sensitivity of the camera was estimated separately for each organ and for each tested shielding configuration by computing the ratio between the number of detected events inside an energy window of twice the energy resolution around the 364-keV photopeak and the number of gamma-rays emitted by the organ. The activity concentration over time in simulated organs was computed by using the compartmental model developed by Leggett, which gives the biokinetics of iodine for euthyroid individuals [36]. The worst case was considered in terms of background noise by setting the 24-h uptake of ^{131}I to 16% in the thyroid, according to data from the ICRP 128 for typical low thyroid uptake of iodine [37]. The different shielding configurations was compared by computing the SNR over time, which is the ratio of the number of detected 364 keV events coming from the thyroid to those coming from the surrounding organs.

V. RESULTS

A. Spectroscopic Performance

The optimization of the energy resolution as a function of the electronics operating parameters, that are the trigger level of the energy branch and the overvoltage applied to the SiPMs, is illustrated on the energy resolution bidimensional plot shown in Fig. 6 (top). An optimal energy resolution of 7.44% FWHM at 356 keV is achieved for a central collimated source with an overvoltage of 7.5 V and a trigger set at 17 DAC units (Fig. 6, bottom). These parameters were chosen as a reference for the operation of the photodetection system. The number of fired pixels per event as a function of the energy and the collected charge is shown in Fig. 7. One can see that the number of fired pixels as a function of collected charge is linear in a certain range, but that the number of fired pixels as a function of the energy is highly nonlinear, resulting in an overall nonlinear response of the detector as a function of the energy deposited in the crystal. The map of the energy resolution and light loss are presented in Fig. 8 (left) and (right), respectively. The mean energy resolution measured in the CFOV is 8.02±0.18% FWHM at 356 keV and degrades to 9.02±0.18% FWHM in the $\overline{\text{CFOV}}$. The mean energy resolution in the UFOV is 8.53±0.59% and
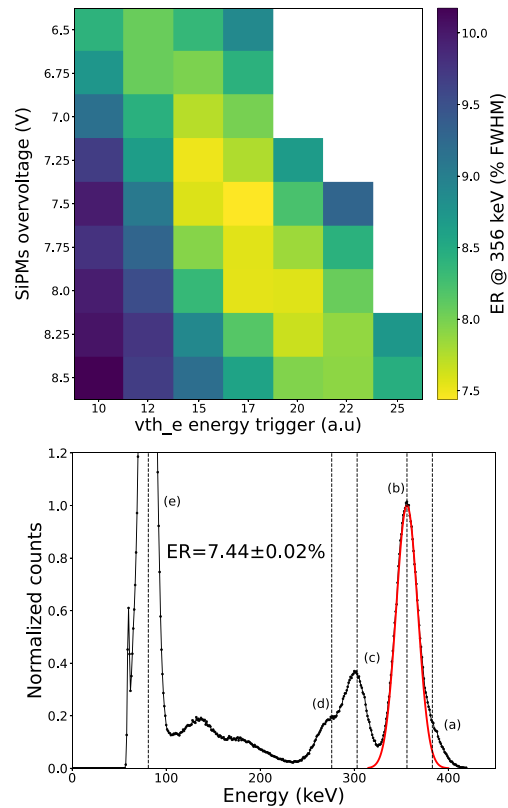

Fig. 6. Top: Energy resolution (ER) at 356 keV in % FWHM as a function of the SiPMs overvoltage and the trigger level of the energy branch. Bottom: ^{133}Ba energy spectrum in the CFOV for the optimal set of electronics parameters. The letters indicate the main gamma emission of ^{133}Ba, that are (a) −383 keV, (b) −356 keV, (c) −302 keV, (d) −276 keV, and (e) -80 keV.
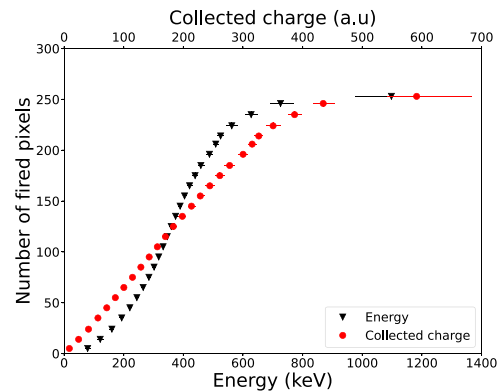

Fig. 7. Number of fired pixels as a function of event energy in keV (black points) and collected charge in arbitrary units (red points). Each point corresponds to the median of the number of fired pixels, energy, and collected charge for each range of ten fired pixels. The errorbars are the first and third quartile of those distributions.

can be compared with the value computed from the flood-field acquisition, which is 8.57% and 11.6% with and without uniformity correction, respectively.

B. Spatial Performance

Fig. 9 shows the scan image (with a step set at 3 mm for readability purpose) performed with the 0.5-mm collimated ^{133}Ba source and the image of a flood-field uniformity
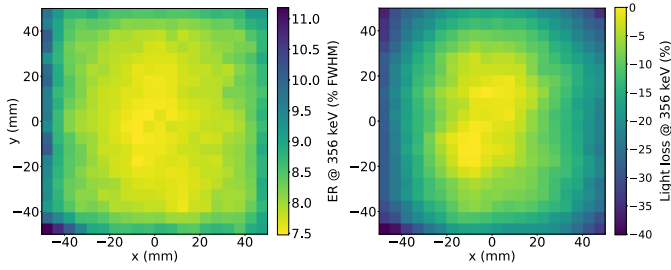
Fig. 8.   Left: Energy resolution (ER) map at 356 keV (% FWHM). Right: Light loss map (% of the maximum position of the 356-keV photopeak). All values were computed from a 5-mm step scan with a ^{133}Ba source.
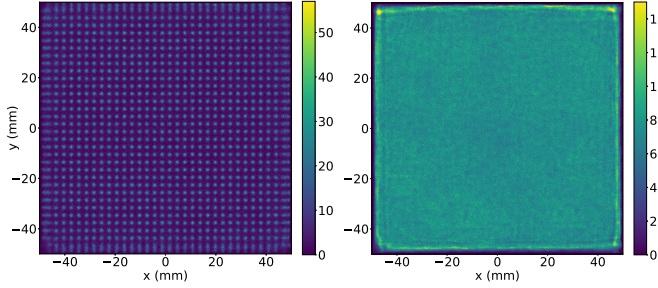

Fig. 9.   Left: Image of a 3-mm step scan performed with a 0.5-mm collimated ^{133}Ba source. Right: Flood-field uniformity image measured with a ^{133}Ba source without collimation.
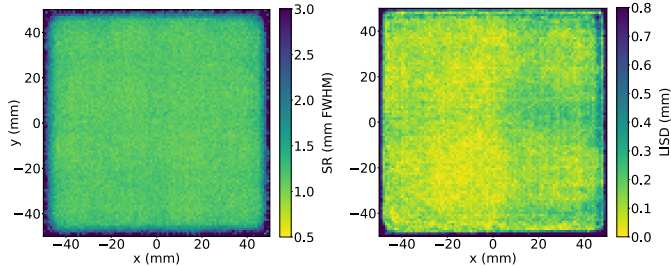

Fig. 10.   Left: Intrinsic SR map. Right: LISD map. All values were computed from a 1-mm step scan with a ^{133}Ba source.

acquired with the ^{133}Ba source without collimation. Both images are reconstructed with the neural network, which provides high spatial performance in the UFOV. The mean intrinsic SR and distortion in the CFOV is 1.15-mm FWHM and 0.11 mm, respectively. Those values only degrade to 1.31-mm FWHM and 0.35 mm in the $\overline{\text{CFOV}}$. The SR and distortion maps reported in Fig. 10 demonstrate that the spatial response is very homogeneous over almost the entire UFOV of the camera. Spatial performance degrades only when approaching within 5 mm of the scintillator edges as shown in Fig. 11 representing the SR and distortion toward the x and y directions for the central row and column of the maps. The bright pixels in the corners of the maps are positions where the fitting algorithm did not converge. The DU value is around 2.5% in the UFOV and is nearly constant on the whole FOV. The IU value measured in the CFOV is 3.35% and increases to 6.3% in the $\overline{\text{CFOV}}$. All spatial performance are summarized in Table I. The neural network reconstruction speed is around 350 events/s/CPU when executed on a Xeon CPU E5-1620 v3 @ 3.50 GHz.
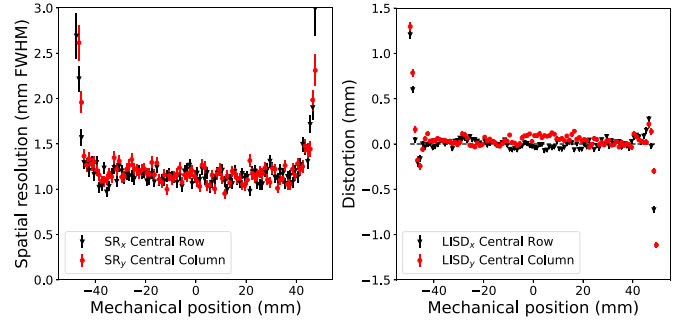

Fig. 11.   Left: Intrinsic SR measured for the central row and column of the scan as a function of the mechanical position of the source. Right: LISD toward the x and y directions measured for the central row and column of the scan, respectively. The error bars are computed from the Gaussian fit uncertainties.

TABLE I
SUMMARY OF THE INTRINSIC SPATIAL PERFORMANCE, INCLUDING SR, LISD, IU, AND DU IN THE UFOV, CFOV, AND $\overline{\text{CFOV}}$ OF THE CAMERA. THE DATA FORMAT IS MEAN±STANDARD DEVIATION COMPUTED FROM SR AND LISD MAPS

	SR (mm)	LISD (mm)	DU (%)	IU (%)
UFOV	1.31±0.40	0.15±0.11	2.45	4.35
CFOV	1.15±0.06	0.11±0.05	2.39	3.35
$\overline{\text{CFOV}}$	1.54±0.55	0.35±0.66	2.47	6.3

C. Counting Rate Performance

Fig. 12 (top) represents the measured counting rate on the whole ^{133}Ba spectrum as a function of the expected counting rate estimated from Monte-Carlo simulation. The linear best fit on the curve shows that the dead time of the camera is negligible up to a counting rate of 160 kcps. We also observed a slight linear degradation of the energy resolution at 356 keV when the measured counting rate increases (Fig. 12, bottom). The red point on the plot corresponds to the mean energy resolution in the UFOV measured at a very low count rate during the measurement of the spatial performance with the 0.5-mm collimated source (see Section III). It confirms that the energy resolution is constant at counting rates below 20 kcps. The slope of the linear fit applied on the increasing part of the curve gives an absolute energy resolution loss of 9.10^{-3}% FWHM/kcps, corresponding to a decrease of the energy resolution from 8.5% FWHM at 18 kcps to 9.7% FWHM at 150 kcps. This effect is associated with a drop of about 8% in the position of the 356-keV photopeak when the measured counting rate increases from 20 to 150 kcps.

D. Influence of Temperature on Energy Response

Fig. 13 (top) represents the variation of the 356-keV photopeak position as a function of the SiPMs temperature with (black) and without (red) correction of the bias voltage relative to the highest photopeak position, obtained at a temperature close to the photodetectors of 21 °C. We observed that the SiPMs temperature is always 4 °C warmer than the ambient temperature (i.e., 21 °C SiPMs=17 °C ambient). The relative variation of the photopeak position is around −4.9%/°C when the SiPMs overvoltage is not adjusted. Thanks to the SiPMs bias voltage correction, the relative fluctuation of the
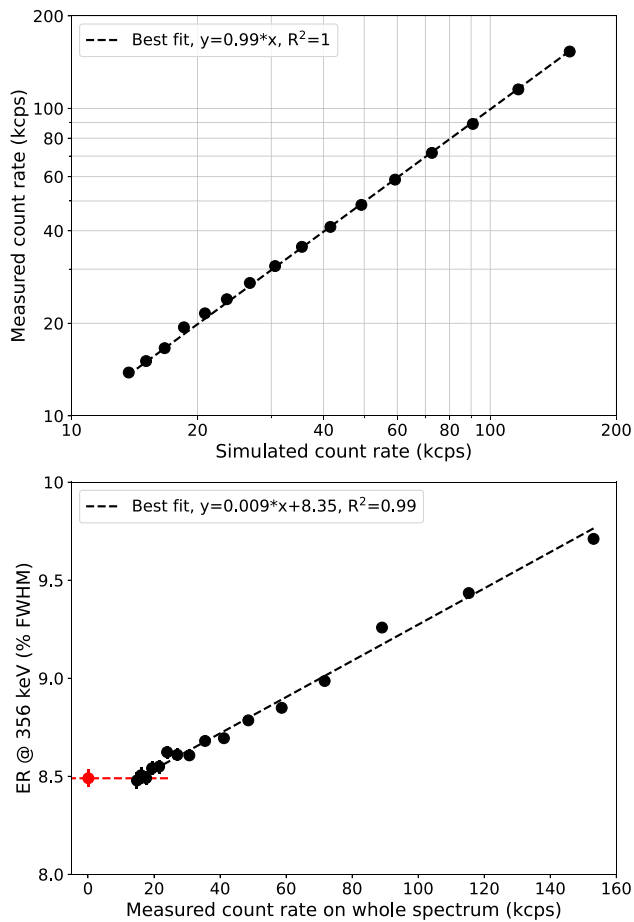
Fig. 12. Top: Measured counting rate (in kcps) as a function of the expected count rate (in kcps) on the whole ^{133}Ba spectrum. The experimental data are represented by black points, while the best linear fit is represented by a dashed line. Bottom: Energy resolution (ER) at 356 keV in % FWHM as a function of the measured count rate on the whole ^{133}Ba spectrum. The black points are computed from the flood-field acquisition at various source–scintillator distances and the red point from the scan with the collimated source. The error bars are computed from the Gaussian fit uncertainties. The best linear fit on the increasing part of the curve is represented by a black dashed line and the plateau region is represented by a red dashed line.
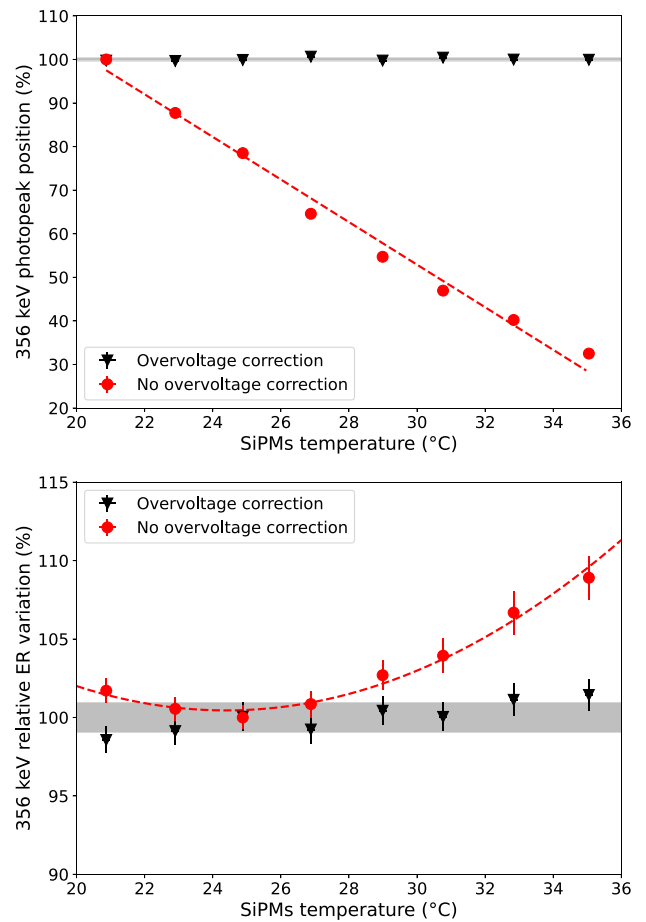

Fig. 13. Top: Relative variation of the 356-keV photopeak position as a function of the SiPMs temperature with (black) and without correction of the bias voltage (red). Bottom: Relative variation of the energy resolution (ER) at 356 keV as a function of the SiPMs temperature with (black) and without correction of the bias voltage (red). The dashed lines are the linear (top) and quadratic (bottom) best fits. The gray region is the $\pm 1\sigma$ band. The error bars on both plots are computed from the Gaussian fit uncertainties.
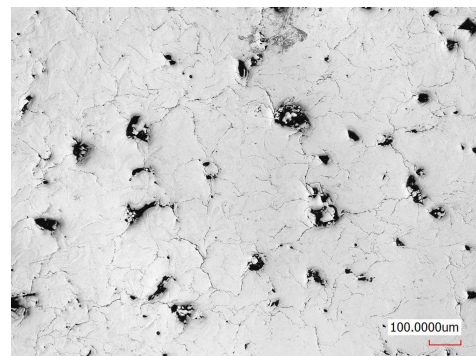
photopeak position is reduced to 0.33%. The variation of the energy resolution as a function of temperature relative to the optimal energy resolution at an ambient temperature of 21 °C does not exceed 10% without voltage correction (Fig. 13, bottom). When the overvoltage of SiPMs is adjusted, the relative fluctuation of the energy resolution at 356 keV is 1.2%.

E. Optimization of the High-Energy Collimator

The optimal printing parameters of the tungsten samples resulted in an envelope density of 18.7 g.cm^{-3}, which is about 97% of the bulk density of tungsten. This value is due to the surface and open porosities which represent 5% of the bulk volume (3.2% and 1.8%, respectively). The size of the open porosities ranges from 1.7 to 2.5 μm. Fig. 14 shows a scanning electron microscope image of a tungsten sample from optimal batch on which one can see surface porosities. The optimal machine parameters correspond to a baseplate heated at 200 °C, a laser power set at 360 W, an exposure

Fig. 14. Scanning electron microscope image of a 3-D printed tungsten sample showing surface porosities.

time of 20 μs, and a distance between spots of 20 μm for a final scanning speed of 0.5 m/s. The width of a bead is about 100 μm and the overlap between two laser paths of 50 μm.

Fig. 15 shows the uE and the SR of the collimator configurations with an eSP of 7.5% corresponding to the 17 hole diameters and 8 collimator lengths simulated. Each point corresponds to a specific combination of hole diameter,
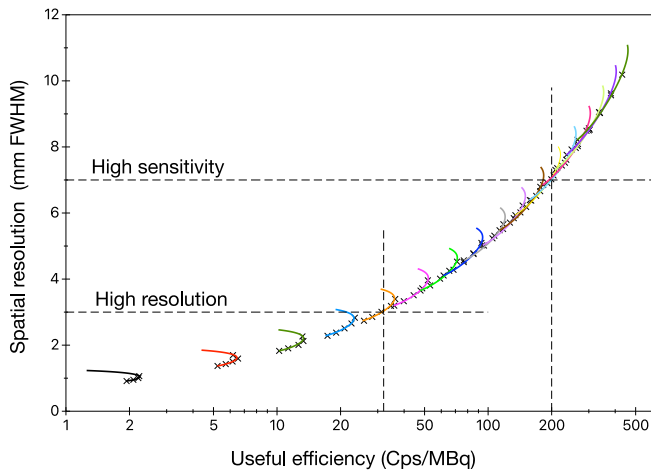
Fig. 15. SR as a function of uE for the geometric configurations of the collimator directly extracted from the simulations (cross) or extrapolated by interpolation from the analytical models (solid line). All configurations are characterized by a septal penetration of 7.5%. Each colored line corresponds to a hole diameter from 0.5 mm (black) to 4.5 mm (green) in 0.25 mm steps and each dot corresponds to a specific combination of hole diameter, collimator length, and septa thickness. The two configurations selected for our application are indicated by a dashed line.

Fig. 16. SNR over time after administration of ^{131}I for all simulated configurations of shielding. *WH-a WTS-b PbT-c* encodes the shielding configuration, where WH is the thickness of tungsten on the front of the camera, WTS is the thickness of tungsten covering the sides of the scintillator, and PbT is the thickness of lead covering the remaining sides and the back of the camera.

collimator length, and septal thickness directly extracted from the simulations. In order to improve clarity, these geometric configurations are gathered by hole diameter using interpolation curves for collimator lengths ranging from 4 to 6.5 cm based on the geometric analytical models. Each color is related to a specific hole diameter, ranging from 0.5 mm (lowest efficiency) to 4.5 mm (highest efficiency). For example, the 1.25-mm hole diameter (interpolated blue curve in Fig. 15) satisfies the requirement of a 7.5% eSP for five simulated configurations characterized by five different lengths from 4.5 cm (higher value of the SR) to 6.5 cm (lower value of the SR) and six septa of decreasing thickness. Among all simulated and interpolated configurations, two collimators with an SR of 3 and 7 mm FWHM were selected in order to meet the specifications of our clinical application. If more than one configuration had the expected SR, the one with the highest uE, which is also generally the smallest septa, was chosen. These two configurations are indicated by a dashed line in Fig. 15. The first configuration dedicated to treatment planning exhibits a high useful sensitivity of 200 cps/MBq and an SR of 7-mm FWHM at a 5-cm distance, which varies at a rate of 0.83 mm per cm of source-to-collimator distance. The second configuration dedicated to post-treatment verification features a high SR of 3-mm FWHM at a 5-cm distance, which varies at a rate of 0.35 mm/cm, and a useful sensitivity of 32 cps/MBq. The high sensitivity and high resolution configurations use a hole diameter of 4.02 and 1.8 mm, a septal thickness of 1.69 and 0.84 mm, and a collimator length of 5.44 and 5.87 cm, respectively.

F. Optimization of the Shielding Geometry

The SNR over time for some simulated shielding configurations is shown in Fig. 16. The shielding configurations are encoded with the name WH-a WTS-b PbT-c, as described in
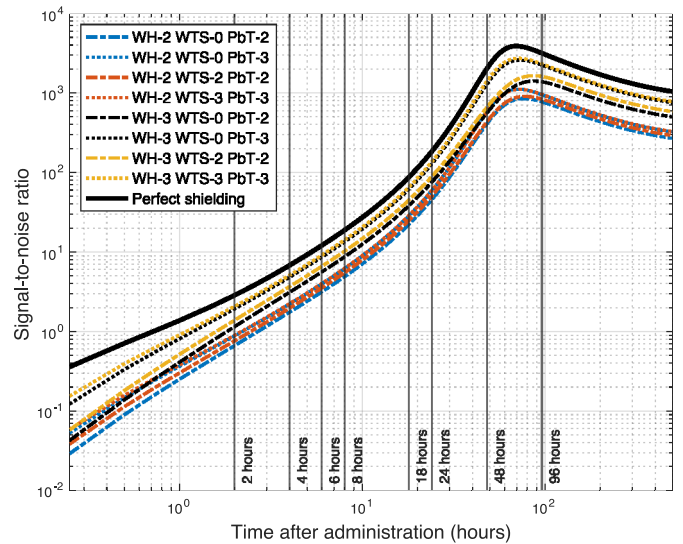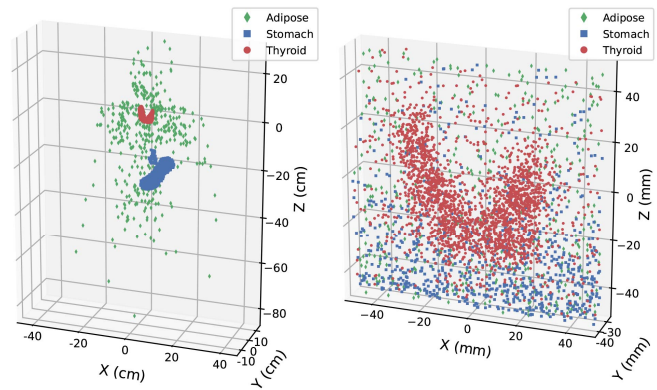

Fig. 17. Left: Emission positions of gamma-rays detected by the camera. Right: Positions of interaction of gamma-rays in the scintillator. Each event is classified according to its region of origin (adipose tissue, stomach, and thyroid). It corresponds to the weakest simulated shielding configuration, WH-2 WTS-0 PbT-2.

Section IV-C and Fig. 2 (center, b). The two main sources of noise when ^{131}I is administered orally are adipose tissues and stomach (Fig. 17, left). These dominant noise sources are correlated with the interaction position of background events in the scintillator, which is almost uniform for events coming from adipose tissues but strongly located in the bottom of the scintillator for events coming from the stomach (Fig. 17, right). Considering those principal noise-source organs and by comparing the SNR of the different geometries to the perfect shielding with infinite density, the optimal geometry in terms of radiation protection and compactness is achieved with a 3-cm thick tungsten plate on the front of the camera, a 3-cm thick tungsten plate covering the sides of the scintillator, and a 3-cm thick lead shielding for the remainder of the sides and the back of the camera (WH-3 WTS-3 PbT-3). At 6 h after treatment administration, this configuration provides an SNR

of 9 compared to a value of 12 for perfect shielding and 3 for the weakest shielding (WH-2 WTS-0 PbT-2).

VI. DISCUSSION

The reported results show the implementation of fast readout electronics and optimized system for the development of a high resolution gamma camera dedicated to dosimetry during radioiodine treatment of thyroid diseases.

The large surface SiPMs array combined with a high-light yield $CeBr_3$ scintillator with reflective coated edges and finely tuned electronics parameters, including SiPMs overvoltage and trigger level, ensure an energy resolution of 8.02% FWHM at 356 keV in the CFOV. Taking into account the segmented nature of the photosensor and the unusually large size of the crystal, this value is relatively close to the energy resolution reported for a $CeBr_3$ crystal block coupled to a PMT (6.6% at 356 keV [38]) and will offer a good rejection of high-energy gamma-rays scattering for a better quantification. The energy response is also very homogeneous on the whole FOV (Fig. 8, left). Indeed, the energy resolution computed on a corrected flood-field energy spectrum (8.57%) is very close to the mean energy resolution measured on the energy scan (8.53% in the UFOV). Its slight degradation to 9.02% on the edges of the FOV is correlated to the light loss, that increases to 40% near the corners of the FOV (Fig. 8, right). The variation of the energy resolution as a function of the trigger level of the energy branch is correlated to two effects. At high threshold levels, the trigger cuts useful signal in the center of the light distribution resulting in a loss of information (Fig. 6, top). At low values of the trigger (below 15 DAC units), all the useful charge is already collected and the pulse height position of the 356-keV photopeak does not increase anymore (data not shown), but the energy resolution degrades. This means that the content of the pixels added to the total charge is dominated by the statistical fluctuation in the tails of the light distribution and by the thermal noise in coincidence with gamma events. The optimum trigger therefore depends on the light distribution on the photodetector and consequently on the incident gamma-ray energy. This results in high nonlinearity of the energy spectrum at low energies when optimizing energy resolution at 356 keV (Fig. 7). Indeed, due to the trigger of the energy branch, the number of fired pixels, which is directly proportional to the measured charge, depends on both the depth of interaction and the energy deposited in the crystal. Between 0 and 300 keV, the mean depth of interaction increases with energy, thus more light is produced with a thinner spatial distribution and the number of fired pixels only slowly increases. Between 300 and 450 keV, the average interaction depth is relatively constant, and the number of triggered SiPMs becomes directly proportional to the energy deposited in the crystal. Above 450 keV, the energy deposited in the crystal is such that the light distribution can trigger all 256 SiPMs simultaneously, which explains why the curve reaches a plateau.

A deep residual CNN has been optimized for ^{131}I imaging in order to reach a mean millimetric intrinsic SR of 1.15-mm FWHM and submillimetric distortion of 0.11 mm in the CFOV. This performance will contribute in reducing partial volume effects for better quantification of small targets and improve overall image quality (Figs. 9 and 10). The spatial response is also very homogeneous over almost the entire FOV, resulting in an effective UFOV of 9×9 cm^2 (Fig. 11). Compared to commercial gamma-cameras, our detector is around three times better in term of intrinsic SR for an equivalent scintillator thickness. Some research teams have investigated the use of neural networks for the same task in PET systems [19], [39], [40]. Our experimental results, obtained at a lower gamma energy, are similar or better than what can be found in the literature, even compared to neural networks trained and tested on simulation data. This is mainly achieved thanks to the special residual architecture we used that improves learning ability and to the quality of our training dataset, that has been carefully filtered to only retain single photoelectric events [18]. Multicompton scattering in the scintillator followed by photoelectric absorption are not correctly reconstructed by the neural network but their contribution remains very low for a 1-cm thick crystal, as described in [18]. The reconstruction rate of 350 events/s/CPU provided by the neural network will allow to reconstruct an appreciable fraction of incoming events in real time, which is very convenient for clinical environment with limited computing resources. As a decrease in complexity of the network degrades its performance but increases its reconstruction rate, it is also possible to use different architectures to adjust reconstruction speed in exchange of SR and distortion.

The counting performance of the camera shows that the loss of counts at rates below 150 kcps is negligible (Fig. 12, top). In the most unfavorable clinical scenario, corresponding to imaging with the optimized high-sensitivity configuration of the collimator (see Section V-E) and high uptake of ^{131}I in the thyroid (maximum value of around 80% reported for Graves' disease 24 h after administration of 800-MBq activity [41]), the expected maximum counting rate on the whole spectrum is less than 40 kcps. Our device is therefore perfectly suited for quantitative imaging during the treatment of thyroid diseases whatever the administrated activity. However, we observed that energy resolution degrades linearly with increasing counting rate above 20 kcps (Fig. 12, bottom). This is due to the operation principle of the electronics. If two gamma events overlap in space (partially trigger the same pixels) and time (in a time window shorter than the maximum triggering rate, i.e., 1/500 kHz=2 μs), the first event will be fully reconstructed, but the pixels triggered by the first event will be missing in the second event. Thus, the second event will be recorded with a lower energy than expected. Less frequently, two events that interact in temporal coincidence (60-ns time window defined for temporal clustering) could be seen as a single event with an overestimated energy and a light distribution composed of two spots. Those two types of events may result in a degradation of the energy resolution and a poor interaction localization, as their morphology differs from events used in the training dataset of the neural network. A mix of those two effects is also possible and leads to a whole family of distorted events at high counting rates. No effect on dead time is observed, as this would require the two temporally

coincident events to completely overlap in space, which is highly unlikely. In theory, given the maximum trigger rate of 500 kHz per channel and a nonparalyzable dead time model, the count loss at 150 kcps would be 23% if gamma events triggered all 256 pixels simultaneously [42]. In reality, when using a ^{133}Ba source, the average number of fired pixels per gamma event is 47 and two successive events rarely completely overlap spatially. Even more, 356 keV events that mobilize the most the electronics and thus would cause most of the dead time, only represent approximately 20% of all measured gammas, the remainder being at lower energies. The nonlinearity of the number of pixels triggered as a function of gamma-ray energy also reduces electronics occupancy by low-energy events, leaving more pixels ready to be triggered by 356-keV gamma-rays (Fig. 7). Another effect that could degrade energy resolution with high counting rates would be a voltage drop across SiPMs due to the relatively high current generated by events. A slight but significant decrease of 8% of the 356-keV peak position is observed when the counting rate increases.

The overall performance of the camera were shown to be nearly insensitive to temperature variations. The energy resolution of the 356-keV photopeak degrades by less than 1% when the ambient temperature varies from 17 °C to 31 °C if a fine tuning of the SiPMs overvoltage as a function the SiPMs temperature is implemented (Fig. 13, bottom). The energy resolution without overvoltage adjustment follows the trend of the energy resolution curve as a function of the SiPMs overvoltage which is linked to the opposing effects of increasing detection efficiency and correlated noises. Air-cooling of the electronics stabilizes the temperature of the whole detection head, making the system more resistant to slight variations of ambient temperature in the clinical environment.

The optimization of the 3-D printing method used to manufacture the tungsten parts of the camera allowed to get an effective density very close to that of pure tungsten (97% of bulk tungsten) and comparable to what is currently achieved in the recent literature [28], [43], [44]. Further improvements can be expected by optimizing the characteristics of the tungsten powder and the printing parameters of the SLM method, which can still be refined to properly print tungsten despite its refractory nature and high melting point. Improving the effective density of the printed material is crucial when imaging high-energy gamma-rays because penetration and scattering in the collimator are responsible for a significant image contrast degradation that reduces source detectability and biases quantification [10]. Beyond the material, optimizing the collimator geometry is also a crucial step in maximizing the SR and sensitivity of the gamma-camera. The significant contribution of penetration and nongeometric scattered events to ^{131}I imaging is clearly visible in Fig. 4. By focusing solely on the contribution of nongeometric events, the eSP parameter we defined is more representative of the impact of penetration and scatter on image contrast (Fig. 5). The 7.5% criterion is also much more restrictive than the usual 5% maximum septal penetration calculated from the attenuation along the shortest path a gamma-ray can travel through a

single septa, which strongly underestimates the contribution of penetration and scatter for high-energy gamma-rays [32], [33]. For example, the estimated penetration from the calculation of the attenuation along the shortest path is 4.7% for a 4.5-cm long collimator with 2-mm diameter holes and 1-mm thick septa when only considering 722-keV energy gamma-rays from ^{131}I, while the simulated value of eSP is more than 47%. This confirms that analytical methods cannot be used to optimize parallel-hole collimators for high-energy gamma-ray imaging. When the geometric opening of the collimator becomes small, corresponding to a ratio between hole diameter and septa thickness less than 1, the eSP reaches a constant value whose intensity decreases with the length of the collimator (Fig. 5). For very small diameter holes, the slow evolution of eSP toward this plateau is slowed down by the increase in the relative contribution of Compton scattering from the high-energy gamma-rays at 636 and 722 keV, which becomes the main component of scattered nongeometric events. All collimator configurations that meet the 7.5% eSP threshold are summarized in Fig. 15. The shape of each colored curve, corresponding to hole of a given diameter, can be understood by noting that the thickness of the septa varies in inverse proportion with the collimator length in order to satisfy the requirement of a 7.5% eSP (the lower part of each curve corresponds to high lengths and small septal thicknesses, while the upper part corresponds to small lengths and higher septal thicknesses). For each hole diameter, the efficiency goes through a maximum when the length of the collimator varies from 4 to 6.5 cm. This means that below a certain collimator length, the significant increase in septa thickness required to maintain a septal penetration at 7.5% results in a decrease in efficiency that is no longer offset by the decrease in collimator length. Taking into account the clinical context in which the camera will be used, two collimator configurations have been chosen to increase the camera's versatility. Both configurations optimize the uE for a given SR. The configuration with high sensitivity and low SR will be used to make images during treatment planning using low administered activities of ^{131}I. When considering a typical activity of 3.7 MBq for planning of hyperthyroidism treatments (Graves' disease, toxic multinodular goiter, or toxic nodule) and a mean uptake of 40% in the thyroid, the expected counting rate in the 364-keV photopeak is 80 cps [41]. The second configuration with high SR will be used for imaging after treatment administration. Despite its low sensitivity, the mean expected counting rate in the 364-keV photopeak is more than several hundred of cps due to the therapeutic activities ranging from 200 to 800 MBq for hyperthyroidism treatments and up to several GBq for thyroid cancers [7], [8]. The expected high global SR of this configuration (around 3.3-mm FWHM at a 5-cm distance by convolving the intrinsic SR of the photodetection system and the geometric resolution of the collimator) will be particularly well suited to accurately quantify the activity in small heterogeneities, such as tumor remnants or nodules, by reducing the partial volume effect. These expected values are slightly overestimated, as the tungsten density and energy resolution used for simulations were deliberately set at the actual bulk tungsten density and

at a very high energy resolution in order to study the intrinsic properties of the collimator, independently of instrumental performance. This approximation does not change the ranking of the different collimator geometries, but slightly reduces the contribution of penetration and scattering coming from high-energy gamma-rays.

In addition to the collimator geometry, the optimization of the detection head shielding is also a key feature when imaging thyroid at short time after ^{131}I administration. The thickness of tungsten on the front of the camera strongly dominates the SNR and WH-3 configurations almost always exhibit better SNR (Fig. 16). Using lead plates to shield the front of the camera was not considered as it would require plates 40% thicker to achieve tungsten-like shielding. This would have enlarged the overall dimensions of the collimator, preventing it from being positioned in contact with the neck, as shown in Fig. 2 (if the front shielding was the same thickness as the collimator, camera positioning would be blocked by the patient's chin and thorax). We observe that at constant thickness, the SNR improvement by using tungsten over lead to shield the sides of the scintillator is marginal. Choosing which material to use is therefore a tradeoff between weight, cost and metal ductility. Conversely, for a given material, an increase of the shielding thickness on the sides of the camera strongly enhances SNR. Indeed, as ^{131}I is administered by oral route, the organ containing the major part of the activity right after treatment administration is the stomach. Therefore, a significant amount of radiations coming from this organ hits the scintillator through the bottom face of the camera (Fig. 17). Considering that, the ranking of the simulated geometries is rather intuitive but the real interest of those simulations lies in the quantitative information they give about the SNR improvement at several times and for different configurations. For instance, at 6 h after ^{131}I administration, a 3 cm rather than 2 cm thick front shielding gives an SNR gain of about 2.3 (8.6 and 4 for WH-3 WTS-0 PbT3 and WH-2 WTS-0 PbT-3, respectively), whereas the same increase for the side shielding gives an SNR gain of 1.6 (8.6 and 5.6 for WH-3 WTS-0 PbT3 and WH-3 WTS-0 PbT-2, respectively). These results also show that the chosen configuration (WH-3 WTS-3 PbT-3) is close to a perfect shielding, as the ratio between those two configurations is nearly constant over time and is around 1.3. It is also interesting to notice that even if the maximum uptake of ^{131}I in the thyroid is reached 24 h after administration, the maximum of SNR is delayed at 70 h due to ^{131}I biokinetics in noise sources, especially in liver, adipose tissue and blood iodide. The finite maximum value of the SNR obtained with the perfect shielding is precisely due to the activity in the blood, which is still detected as part of it is contained within the FOV.

VII. CONCLUSION

The high-resolution portable gamma-camera we developed and optimized fully satisfies the clinical requirements for estimation of absorbed dose during radioiodine treatment of thyroid diseases. The energy resolution of 8.53% at 356 keV, millimetric intrinsic SR, submillimetric distortion and

high counting rate capability should give access to accurate quantitative imaging. The neural network image reconstruction offers a processing speed of 350 events/s/CPU that is suitable for real time monitoring in clinical conditions. Thanks to the optimization of the SLM method and Monte-Carlo simulations, the features of the parallel-hole collimators and shielding were optimized to improve further the image quality. The pair of collimators increases the versatility of the gamma-camera for both planning and post-treatment control by allowing imaging for a large range of activities and times after treatment administration. The fully integrated gamma camera will be accurately calibrated with the two parallel-holes collimators thanks to geometrical ^{131}I sources and its quantification capability will be assessed on 3-D printed thyroid phantoms. After optimization of the quantification protocol, the clinical impact of our device will be evaluated on patients with different pathologies during a prospective clinical trial.

DECLARATION OF COMPETING INTEREST

All authors declare that they have no known conflicts of interest in terms of competing financial interests or personal relationships that could have an influence or are relevant to the work reported in this article.

ACKNOWLEDGMENT

REFERENCES

[1] T. Das and S. Banerjee, "Theranostic applications of lutetium-177 in radionuclide therapy," *Current Radiopharm.*, vol. 9, no. 1, pp. 94–101, 2016.

[2] M. R. Alam, S. B. Singh, S. Thapaliya, S. Shrestha, S. Deo, and K. Khanal, "A review of 177 lutetium-PSMA and 225 actinium-PSMA as emerging theranostic agents in prostate cancer," *Cureus*, vol. 14, no. 9, Sep. 2022, Art. no. e29369, doi: 10.7759/cureus.29369.

[3] L. Lezaic et al., "[111In]In-CP04 as a novel cholecystokinin-2 receptor ligand with theranostic potential in patients with progressive or metastatic medullary thyroid cancer: Final results of a GRAN-T-MTC Phase I clinical trial," *Eur. J. Nucl. Med. Mol. Imag.*, vol. 50, pp. 892–907, Feb. 2023, doi: 10.1007/s00259-022-05992-6.

[4] K. S. Gleisner et al., "Variations in the practice of molecular radiotherapy and implementation of dosimetry: Results from a European survey," *EJNMMI Phys.*, vol. 4, no. 1, p. 28, Dec. 2017, doi: 10.1186/s40658-017-0193-4.

[5] U. Eberlein, M. Cremonesi, and M. Lassmann, "Individualized dosimetry for theranostics: Necessary, nice to have, or counterproductive?" *J. Nucl. Med.*, vol. 58, no. S2, pp. 97S–103S, Sep. 2017, doi: 10.2967/jnumed.116.186841.

[6] L. Strigari et al., "The evidence base for the use of internal dosimetry in the clinical practice of molecular radiotherapy," *Eur. J. Nucl. Med. Mol. Imag.*, vol. 41, no. 10, pp. 1976–1988, Oct. 2014, doi: 10.1007/s00259-014-2824-5.

[7] D. Van Nostrand and L. Wartofsky, "Radioiodine in the treatment of thyroid cancer," *Endocrinol. Metabolism Clin. North America*, vol. 36, no. 3, pp. 807–822, Sep. 2007, doi: 10.1016/j.ecl.2007.04.006.

[8] A. P. Weetman, "Radioiodine treatment for benign thyroid diseases," *Clin. Endocrinol.*, vol. 66, no. 6, pp. 757–764, Jun. 2007, doi: 10.1111/j.1365-2265.2007.02841.x.

[9] E. Rault, S. Vandenberghe, R. Van Holen, J. De Beenhouwer, S. Staelens, and I. Lemahieu, "Comparison of image quality of different iodine isotopes (I-123, I-124, and I-131)," *Cancer Biother. Radiopharmaceut.*, vol. 22, no. 3, pp. 423–430, Jun. 2007, doi: 10.1089/cbr.2006.323.

[10] L. P. Clarke, C. B. Saw, L. K. Leong, and A. N. Serafini, "SPECT imaging of 131I (364 keV): Importance of collimation," *Nucl. Med. Commun.*, vol. 6, no. 1, pp. 41–48, Jan. 1985, doi: 10.1097/00006231-198501000-00007.

[11] A. C. Perkins and J. E. Lees, *Gamma Cameras for Interventional and Intraoperative Imaging* (Series in Medical Physics and Biomedical Engineering). Boca Raton, FL, USA: CRC Press/Taylor Francis Group, 2017.

[12] Y.-J. Jung et al., "Development of a sub-miniature gamma camera for multimodal imaging system," *Nucl. Instrum. Methods Phys. Res. A, Accelerators, Spectrometers, Detectors Assoc. Equip.*, vol. 954, Feb. 2020, Art. no. 161705, doi: 10.1016/j.nima.2018.12.020.

[13] R. Massari, A. Ucci, C. Campisi, F. Scopinaro, and A. Soluri, "A novel fully integrated handheld gamma camera," *Nucl. Instrum. Methods Phys. Res. A, Accel. Spectrometers, Detect. Assoc. Equip.*, vol. 832, pp. 271–278, Oct. 2016, doi: 10.1016/j.nima.2016.06.124.

[14] N. Dinu et al., "SiPM arrays and miniaturized readout electronics for compact gamma camera," *Nucl. Instrum. Methods Phys. Res. A, Accel. Spectrometers, Detect. Assoc. Equip.*, vol. 787, pp. 367–372, Jul. 2015, doi: 10.1016/j.nima.2015.01.083.

[15] A. H. Ng, M. S. Alqahtani, L. K. Jambi, S. L. Bugby, J. E. Lees, and A. C. Perkins, "Assessing a small field of view hybrid gamma camera for perioperative iodine-125 seed localisation," *BJR*, vol. 92, no. 1098, Apr. 2019, Art. no. 20190020, doi: 10.1259/bjr.20190020.

[16] C. Trigila et al., "A mobile high-resolution gamma camera for therapeutic dose control during radionuclide therapy," *Phys. Med. Biol.*, vol. 67, no. 3, Jan. 2022, Art. no. 35011, doi: 10.1088/1361-6560/ac4c31.

[17] A. D. Giovanni et al., "Characterisation of a CeBr3 (LB) detector for space application," *J. Inst.*, vol. 14, no. 9, p. 9017, Sep. 2019, doi: 10.1088/1748-0221/14/09/P09017.

[18] T. Bossis et al., "Optimized reconstruction of the position of interaction in high-performances γ-cameras," *Nucl. Instrum. Methods Phys. Res. A, Accel., Spectromet., Detect. Assoc. Equip.*, vol. 1048, Mar. 2023, Art. no. 167907, doi: 10.1016/j.nima.2022.167907.

[19] G. Jaliparthi, P. F. Martone, A. V. Stolin, and R. R. Raylman, "Deep residual-convolutional neural networks for event positioning in a monolithic annular PET scanner," *Phys. Med. Biol.*, vol. 66, no. 14, Jul. 2021, Art. no. 145008, doi: 10.1088/1361-6560/ac0d0c.

[20] K. He, X. Zhang, S. Ren, and J. Sun, "Deep residual learning for image recognition," Dec. 2015, *arXiv:1512.03385*.

[21] *NEMA Standards Publication NU 1-2018, Performance Measurements of Gamma Cameras*, Nat. Electr. Manuf. Assoc., Arlington, VA, USA, 2019.

[22] B. S. Bhatia, S. L. Bugby, J. E. Lees, and A. C. Perkins, "A scheme for assessing the performance characteristics of small field-of-view gamma cameras," *Physica Medica*, vol. 31, no. 1, pp. 98–103, 2015, doi: 10.1016/j.ejmp.2014.08.004.

[23] S. H. Lee and R. P. Gardner, "A new G–M counter dead time model," *Appl. Radiat. Isotopes*, vol. 53, nos. 4–5, pp. 731–737, Nov. 2000, doi: 10.1016/S0969-8043(00)00261-X.

[24] D. Sarrut et al., "Advanced Monte Carlo simulations of emission tomography imaging systems with GATE," *Phys. Med. Biol.*, vol. 66, no. 10, May 2021, Art. no. 10TR03, doi: 10.1088/1361-6560/abf276.

[25] J. M. Berger. "NISTXCOM: Photon cross section database." 2010. [Online]. Available: http://www.nist.gov/pml/data/xcom/index.cfm

[26] J. I. Gear, J. Taprogge, O. White, and G. D. Flux, "Characterisation of the attenuation properties of 3D-printed tungsten for use in gamma camera collimation," *EJNMMI Phys.*, vol. 6, no. 1, p. 1, Dec. 2019, doi: 10.1186/s40658-018-0238-3.

[27] A. Razavykia, E. Brusa, C. Delprete, and R. Yavari, "An overview of additive manufacturing technologies—A review to technical synthesis in numerical study of selective laser melting," *Materials*, vol. 13, no. 17, p. 3895, Jan. 2020, doi: 10.3390/ma13173895.

[28] A. Iveković et al., "Selective laser melting of tungsten and tungsten alloys," *Int. J. Refractory Metals Hard Mater.*, vol. 72, pp. 27–32, Apr. 2018, doi: 10.1016/j.ijrmhm.2017.12.005.

[29] X. Zhou, X. Liu, D. Zhang, Z. Shen, and W. Liu, "Balling phenomena in selective laser melted tungsten," *J. Mater. Process. Technol.*, vol. 222, pp. 33–42, Aug. 2015, doi: 10.1016/j.jmatprotec.2015.02.032.

[30] J. Huang, M. Li, J. Wang, Z. Pei, P. Mclntyre, and C. Ma, "Selective laser melting of tungsten: Effects of hatch distance and point distance on pore formation," *J. Manuf. Processes*, vol. 61, pp. 296–302, Jan. 2021, doi: 10.1016/j.jmapro.2020.11.034.

[31] K.-I. Mukaida, "Density measurement of small porous particles by mercury porosimetry," *Powder Technol.*, vol. 29, no. 1, pp. 99–107, 1981, doi: 10.1016/0032-5910(81)85008-5.

[32] R. L. Mather, "Gamma-ray collimator penetration and scattering effects," *J. Appl. Phys.*, vol. 28, no. 10, pp. 1200–1207, Oct. 1957, doi: 10.1063/1.1722607.

[33] H. O. Anger, "Scintillation camera with multichannel collimators," *J. Nucl. Med.*, vol. 5, pp. 515–531, Jul. 1964.

[34] E. Keller, "Optimum dimensions of parallel-hole, multi-aperture collimators for gamma-ray cameras," *J. Nucl. Med.*, vol. 9, no. 6, pp. 233–235, 1968

[35] W. P. Segars, G. Sturgeon, S. Mendonca, J. Grimes, and B. M. W. Tsui, "4D XCAT phantom for multimodality imaging research: 4D XCAT phantom for multimodality imaging research," *Med. Phys.*, vol. 37, no. 9, pp. 4902–4915, 2010, doi: 10.1118/1.3480985.

[36] R. W. Leggett, "A physiological systems model for iodine for use in radiation protection," *Radiat. Res.*, vol. 174, no. 4, pp. 496–516, 2010, doi: 10.1667/RR2243.1.

[37] S. Mattsson et al., "ICRP Publication 128: Radiation dose to patients from radiopharmaceuticals: A compendium of current information related to frequently used substances," *Ann. ICRP*, vol. 44, no. S2, pp. 7–321, 2015, doi: 10.1177/0146645314558019.

[38] P. Guss, M. Reed, D. Yuan, M. Cutler, C. Contreras, and D. Beller, "Comparison of CeBr 3 with LaBr3:Ce, LaCl3:Ce, and NaI:Tl detectors," in *Proc. Hard X-Ray, Gamma-Ray, Neutron Detect. Phys. XII*, 2010, Art. no. 78050L, doi: 10.1117/12.862579.

[39] A. Iborra, A. J. González, A. González-Montoro, A. Bousse, and D. Visvikis, "Ensemble of neural networks for 3D position estimation in monolithic PET detectors," *Phys. Med. Biol.*, vol. 64, no. 19, Oct. 2019, Art. no. 195010, doi: 10.1088/1361-6560/ab3b86.

[40] W. He et al., "A preliminary study on 3D position reconstruction of monolithic crystal readout," *Radiat. Detect. Technol. Methods*, vol. 5, no. 1, pp. 102–109, Mar. 2021, doi: 10.1007/s41605-020-00225-6.

[41] C. Happel et al., "Thyroid stunning in radioiodine-131 therapy of benign thyroid diseases," *Endocrine*, vol. 63, no. 3, pp. 537–544, Mar. 2019, doi: 10.1007/s12020-018-01833-5.

[42] J. W. Müller, "Dead-time problems," *Nucl. Instrum. Methods*, vol. 112, nos. 1–2, pp. 47–57, Sep. 1973, doi: 10.1016/0029-554X(73)90773-8.

[43] Z. Xiong, P. Zhang, C. Tan, D. Dong, W. Ma, and K. Yu, "Selective laser melting and remelting of pure tungsten," *Adv. Eng. Mater.*, vol. 22, no. 3, Mar. 2020, Art. no. 1901352, doi: 10.1002/adem.201901352.

[44] C. Tan, K. Zhou, W. Ma, B. Attard, P. Zhang, and T. Kuang, "Selective laser melting of high-performance pure tungsten: Parameter design, densification behavior and mechanical properties," *Sci. Technol. Adv. Mater.*, vol. 19, no. 1, pp. 370–380, Dec. 2018, doi: 10.1080/14686996.2018.1455154.